Identifying Objects at the Quantum Limit for Superresolution Imaging

Michael R. Grace and Saikat Guha

James C. Wyant College of Optical Sciences, University of Arizona, Tucson, Arizona 85721, USA

We consider passive imaging tasks involving discrimination between known candidate objects and investigate the best possible accuracy with which the correct object can be identified. We analytically compute quantum-limited error bounds for hypothesis tests on *any* library of incoherent, quasimonochromatic objects when the imaging system is dominated by optical diffraction. We further show that object-independent linear-optical spatial processing of the collected light exactly achieves these ultimate error rates, exhibiting scaling superior to spatially resolved direct imaging as the scene becomes more severely diffraction limited. We apply our results to example imaging scenarios and find conditions under which superresolution object discrimination can be physically realized.

Introduction.—Object discrimination is at the heart of decision making in medical diagnostics, extrasolar astronomy, and autonomous sensing. For incoherent imaging with large standoff distances, small objects, and/or a small aperture, optical diffraction impedes accurate discrimination between spatially distinct objects. A classic heuristic criterion, attributed to Rayleigh, holds that two objects cannot be discriminated when their distinguishing features exhibit length scales smaller than the width of the system's point-spread-function (PSF) [1]. More quantitatively, for hypothesis tests between such "sub-Rayleigh" objects, the probability of correct identification degrades as the PSF more severely perturbs the measured images [2].

A paradigm shift for sub-Rayeigh imaging recently emerged via the calculation of task-specific error bounds that optimize over all measurements permitted by quantum mechanics [3]. These "quantum limits" revealed that direct measurements of the image-plane optical intensity profile are responsible for the catastrophic degree of error implied by the Rayleigh criterion, whereas alternative measurements yield far lower error than direct imaging for many tasks [4–8]. Quantum limits, and "quantum-optimal" measurements that achieve them, were found for specific hypothesis tests including one-vs-two point source discrimination [9,10] and exoplanet detection [11,12]. However, no general results exist that broadly apply to real-world object discrimination settings.

This Letter finds quantum limits and quantum-optimal measurements for generalized sub-Rayleigh object discrimination, with applicability to subcellular fluorescence microscopy, exoplanet surveys, pattern recognition in remote sensing, and many more imaging domains. For sub-Rayleigh hypothesis tests between *any* two incoherent, quasimonochromatic 2D objects, we (1) compute the quantum Chernoff bound on symmetric discrimination error, (2) compute the classical Chernoff exponent that

characterizes the error obtained with ideal direct imaging, (3) quantify a quadratic scaling gap between the two Chernoff exponents, and (4) identify a quantum-optimal measurement that employs a predetection spatial-mode sorting device whose linear-optical design does not depend on the objects. Remarkably, our results extend to *M*-ary discrimination: the same object-independent measurement is quantum-optimal for *any* $M > 2$ sub-Rayleigh objects. Last, we define Hamming-like distance measures for object libraries to quantify the realizable advantage over direct imaging.

Quantum model.—Let the label H_j, $j \in [1, M]$, denote a hypothesis corresponding to one of M candidate objects. Under hypothesis H_j, the quantum state η_j on Hilbert space $\mathcal{H}$ describes one temporal mode of a quasimonochromatic optical field collected by an imaging system. Many natural thermal sources exhibit $\epsilon \ll 1$ mean photons per temporal mode such that multiphoton detection within the optical coherence time is vanishingly rare [13]. Using a weak-source Fock expansion $\eta_j = (1 - \epsilon)|0\rangle\langle 0| + \epsilon\rho_j + O(\epsilon^2)$, where $|0\rangle\langle 0|$ is the vacuum state, the state ρ_j carries all spatial information about the *j*th object [4]. Since ρ_j models one photon over multiple orthogonal spatial modes, it can be mapped onto a Hilbert space spanned by the Fock states of a single bosonic mode [4]. We denote this Hilbert space $\mathcal{H}^{(1)}$.

Let an imaging system with a 2D coherent PSF $\psi(\vec{x})$ relate object- and image-plane position vectors $\vec{x}_{\text{obj}} = \{x_{\text{obj}}, y_{\text{obj}}\}$ and $\vec{x} = \mu\vec{x}_{\text{obj}}$ by the transverse magnification μ. We spatially model the object under hypothesis H_j by a normalized radiant exitance profile $m_j(\vec{x}_{\text{obj}})$. The state of the collected optical field on $\mathcal{H}^{(1)}$ is then [14]

$$\rho_j = \int \int_{-\infty}^{\infty} \frac{1}{\mu^2} m_j\left(\frac{\vec{x}}{\mu}\right) |\psi_{\vec{x}}\rangle\langle\psi_{\vec{x}}| d^2\vec{x}, \qquad (1)$$
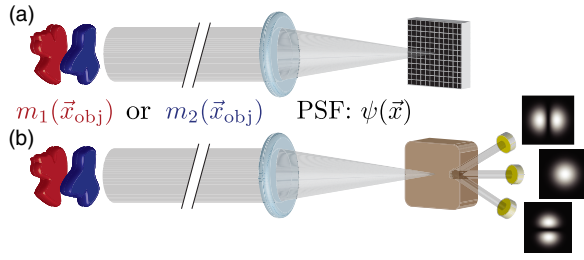
FIG. 1. Discrimination of two objects $m_1(\vec{x}_{\mathrm{obj}})$ and $m_2(\vec{x}_{\mathrm{obj}})$. (a) Direct imaging. (b) TRISPADE receiver using a spatial-mode sorter and three shot-noise-limited photon detectors. For a 2D Gaussian PSF, the sorted modes are shown at right.

where the pure state $|\psi_{\vec{x}}\rangle = \int \int_{-\infty}^{\infty} \psi(\vec{a} - \vec{x})|\vec{a}\rangle d^2\vec{a}$ encodes the effect of the aperture and $|\vec{x}\rangle$ is a single-photon eigenket at image-plane position $\vec{x}$ [4]. In a basis of orthogonal vectors $|\phi_m\rangle = \int \int_{-\infty}^{\infty} \phi_m(\vec{x})|\vec{x}\rangle d^2\vec{x}$ that span $\mathcal{H}^{(1)}$, where $\phi_m(\vec{x})$ are orthogonal 2D functions, the density matrix

$$\rho_j = \sum_{m,n=0}^{\infty} d_{j,m,n}|\phi_m\rangle\langle\phi_n| \qquad (2)$$

has elements $d_{j,m,n} = \int \int_{-\infty}^{\infty} \mu^{-2} m_j(\vec{x}/\mu) c_{m,n}(\vec{x}) d^2\vec{x}$, where $c_{m,n}(\vec{x}) = \langle\phi_m|\psi_{\vec{x}}\rangle\langle\psi_{\vec{x}}|\phi_n\rangle$.

Quantum and classical detection theory.—Consider a hypothesis test between objects $m_1(\vec{x}_{\mathrm{obj}})$ and $m_2(\vec{x}_{\mathrm{obj}})$ with equal prior probabilities (Fig. 1). To decide between hypotheses H_1 and H_2, a receiver measures the true state $\eta_1^{\otimes\mathcal{M}}$ or $\eta_2^{\otimes\mathcal{M}}$ acquired over $\mathcal{M}$ temporal modes and applies a predetermined decision rule on the outcome(s). If the conditional probability of deciding $H_{j'}$ under true hypothesis H_j is $P(\text{say } H'_j|H_j \text{ true})$, the average error probability $P_{\mathrm{err}} = [P(\text{say } H_1|H_2 \text{ true}) + P(\text{say } H_2|H_1 \text{ true})]/2$ is a symmetric performance metric [15] for that measurement and decision rule [17]. Optimizing over all such schemes, the quantum-limited minimum average error probability $P_{\mathrm{err}}^{\min} \sim e^{-\xi_Q \mathcal{M}}$ follows an exponential decay when $\mathcal{M} \gg 1$, where the quantum Chernoff exponent (QCE) ξ_Q quantifies how efficiently each additional copy of the received state η_j suppresses the minimum error [18,19]. Under the weak-source model, this minimum error decays as $P_{\mathrm{err}}^{\min} \sim e^{-\xi_Q^{(1)} N}$, where $N = \epsilon\mathcal{M}$ is the average photon number of $\eta_j^{\otimes\mathcal{M}}$. In the Supplemental Material [22], we show that the per-photon QCE [18,19]

$$\xi_Q^{(1)} = -\log\left[\min_{0 \leq s \leq 1} \mathrm{Tr}(\rho_1^s \rho_2^{1-s})\right] \qquad (3)$$

obeys $\xi_Q \approx \epsilon\xi_Q^{(1)}$ for weak-source sub-Rayleigh objects.

The most general description of a measurement, a positive operator-valued measure (POVM), consists of a set of positive semidefinite operators $\{\Pi_z\}_{\mathcal{Z}}$ on $\mathcal{H}$, linked to measurement outcomes z in an outcome space $\mathcal{Z}$, that

resolve the identity operator as $\sum_{z \in \mathcal{Z}} \Pi_z = \mathcal{I}$ [20]. For a particular measurement performed on $\eta_j^{\otimes\mathcal{M}}$, the minimum average error among all decision rules goes as $P_{\mathrm{err,meas}}^{\min} \sim e^{-\xi_{\mathrm{meas}}\mathcal{M}}$, where ξ_{meas} is the Chernoff exponent (CE) for that measurement [17,21]. For weak sources, the minimal error of any photon-counting measurement goes as $P_{\mathrm{err,meas}}^{\min} \sim e^{-\xi_{\mathrm{meas}}^{(1)} N}$ [22], where $\xi_{\mathrm{meas}} \approx \epsilon\xi_{\mathrm{meas}}^{(1)}$ in the sub-Rayleigh regime and where

$$\xi_{\mathrm{meas}}^{(1)} = -\log\left[\min_{0 \leq s \leq 1} \sum_{z \in \mathcal{Z}^{(1)}} P(z|\rho_1)^s P(z|\rho_2)^{1-s}\right] \qquad (4)$$

is the per-photon CE [17], which depends on the single-photon outcome probabilities $P(z|\rho_j) = \mathrm{Tr}(\Pi_z^{(1)}\rho_j)$ obtained by the reduced POVM $\{\Pi_z^{(1)}\}_{\mathcal{Z}^{(1)}}$ on $\mathcal{H}^{(1)}$ with outcomes $z \in \mathcal{Z}^{(1)}$.

The quantum and classical statistics are related by the quantum Chernoff bound $\xi_{\mathrm{meas}} \leq \xi_Q$, i.e., the QCE automatically optimizes over the CEs of all POVMs on $\mathcal{H}^{\otimes\mathcal{M}}$ [27]. A measurement whose CE matches the QCE ($\xi_{\mathrm{meas}}^{(1)} = \xi_Q^{(1)}$) is quantum optimal for the given hypothesis test. Conversely, a gap ($\xi_{\mathrm{meas}}^{(1)} < \xi_Q^{(1)}$) indicates a fundamental sub-optimality in the measurement that cannot be remedied by data postprocessing.

Results: binary object discrimination.—In this section we compute the QCE $\xi_Q^{(1)}$ for generalized sub-Rayleigh object discrimination and find a universally optimal measurement for which $\xi_{\mathrm{meas}}^{(1)} = \xi_Q^{(1)}$. For a preliminary result, if the object under H_1 is a single point source at object-plane position $\vec{x}_{1,\mathrm{obj}} = \vec{x}_1/\mu$, as in Refs. [9–12], then for any second object the QCE is [22]

$$\xi_Q^{(1)} = -\log\left[\int \int_{-\infty}^{\infty} \frac{1}{\mu^2} m_2\left(\frac{\vec{x} - \vec{x}_1}{\mu}\right)|\Gamma(\vec{x})|^2 d^2\vec{x}\right], \qquad (5)$$

where $\Gamma(\vec{x}) = \langle\psi_{\vec{\Omega}}|\psi_{\vec{x}}\rangle = \int \int_{-\infty}^{\infty} \psi^*(\vec{a})\psi(\vec{a} - \vec{x}) d^2\vec{a}$ is the 2D autocorrelation function of the PSF and $\vec{\Omega} = \{0,0\}$ denotes the origin in the image plane. This quantum limit is achieved (i.e., $\xi_{\mathrm{BSPADE}}^{(1)} = \xi_Q^{(1)}$) by a 2D binary spatial mode demultiplexing (BSPADE) device [4,28,29] that passively couples a PSF-matched spatial mode to one shot-noise-limited photon-counting detector ($\Pi_0 = |\psi_{\vec{x}_1}\rangle\langle\psi_{\vec{x}_1}|$) and all other light to a second detector ($\Pi_1 = \mathcal{I} - |\psi_{\vec{x}_1}\rangle\langle\psi_{\vec{x}_1}|$) [22]. Equation (5) is an exact expression for the QCE of any point-source-vs-known-object hypothesis test, sub-Rayleigh or otherwise, and BSPADE is always quantum optimal in this case.

We now generalize to two arbitrary objects $m_1(\vec{x}_{\mathrm{obj}})$ and $m_2(\vec{x}_{\mathrm{obj}})$ and obtain analytical results in the sub-Rayleigh regime. Define $\gamma = \mu\theta/\sigma$ as the magnification-scaled geometric ratio between the largest spatial extent among the
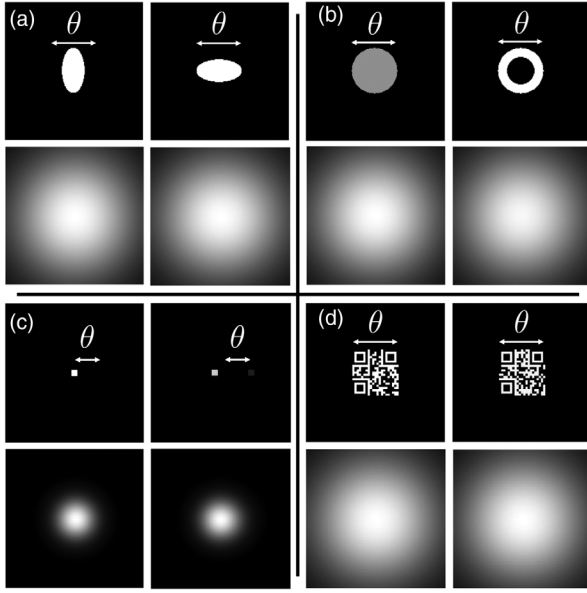
FIG. 2. Simplified object pair examples. (a) Vertical vs horizontal ellipse. (b) Filled vs hollow nuclear pore [33]. (c) Exoplanet detection. (d) QR code reading. Upper images: normalized ground truth object irradiance. Lower images: Gaussian-PSF-convolved image-plane intensity profiles when $\gamma = 1$.

objects (θ) vs the PSF width (σ). The sub-Rayleigh limit $\gamma \ll 1$ is of greatest interest for superresolution imaging, as diffraction significantly impairs conventional object distinguishability below $\gamma = 1$ (Fig. 2). We also define $\tilde{m}_j(\vec{x}_{\mathrm{obj}}) = \theta^2 m_j(\theta\vec{x}_{\mathrm{obj}})$, $\tilde{\psi}(\vec{x}) = \sigma\psi(\sigma\vec{x})$, and $\tilde{\Gamma}(\vec{x}) = \Gamma(\sigma\vec{x})$ to rescale and nondimensionalize the objects, PSF, and PSF autocorrelation function, isolating the effect of γ from that of the object and PSF shapes [22]. We require that the objects' 2D centroids coincide at a location known to the receiver such that the task is object identification and not localization [30–32] and that the PSF $\psi(\vec{x})$ is even in x and y (e.g., a circularly symmetric aperture).

To derive the generalized QCE [22], we represent ρ_j [Eq. (2)] in a basis of PSF-adapted (PAD) eigenvectors $|\phi_m\rangle$ via Gram-Schmidt orthogonalization of the 2D Cartesian derivatives of the PSF [34–36]. For a Gaussian PSF $\psi(\vec{x}) = (2\pi\sigma^2)^{-1/2}\exp[-(x^2+y^2)/4\sigma^2]$, the PAD basis functions $\phi_m(\vec{x})$ are Hermite-Gauss polynomials [35]. After expanding ρ_1 and ρ_2 in powers of $\gamma \ll 1$ and truncating to finite dimensions [5], we use operator perturbation theory [16] to find

$$\xi_Q^{(1)} = \max_{0 \le s \le 1}[(sm_{1,x^2} + (1-s)m_{2,x^2} - m_{1,x^2}^s m_{2,x^2}^{1-s})\Gamma_{x^2}$$
$$+ (sm_{1,y^2} + (1-s)m_{2,y^2} - m_{1,y^2}^s m_{2,y^2}^{1-s})\Gamma_{y^2}]\gamma^2 + O(\gamma^3),$$
(6)

where $m_{j,x^k y^l} = \int\int_{-\infty}^{\infty} x_{\mathrm{obj}}^k y_{\mathrm{obj}}^l \tilde{m}_j(\vec{x}_{\mathrm{obj}})d^2\vec{x}_{\mathrm{obj}}$ are spatial moments of the object models and $\Gamma_{x^k y^l} = -\{\mathrm{Re}[\partial^{k+l}\tilde{\Gamma}(\vec{x})/\partial x^k \partial y^l]\}_{\vec{x}=\vec{\Omega}}$ are derivatives of the PSF

autocorrelation function. The QCE in Eq. (6) is our first main result and represents the quantum limit for discrimination between *any* two incoherent objects in the sub-Rayleigh limit $\gamma \ll 1$. Important features of Eq. (6) include the $O(\gamma^2)$ scaling of the QCE and the separable contributions from the object second moments and the second derivatives of $\tilde{\Gamma}(\vec{x})$. Moreover, the minimization over powers of infinite-dimensional matrices [Eq. (3)] is replaced with a simple maximization of a scalar function.

We compute the CE for ideal direct imaging [i.e., infinite spatial bandwidth, unity fill factor, unity quantum efficiency, Fig. 1(a)] with a zeroless PSF [37] that is separable in x and y to be [22]

$$\xi_{\mathrm{direct}}^{(1)} = (1/32)(\mathcal{K}_x + \mathcal{K}_y)\gamma^4 + O(\gamma^5),$$
(7)

with $\mathcal{K}_a = (m_{1,a^2} - m_{2,a^2})^2 \int\int_{-\infty}^{\infty} \psi_{a^2}(\vec{x})^2/|\tilde{\psi}(\vec{x})|^2 d^2\vec{x}$ for $a \in [x,y]$ and where $\psi_{x^k y^l}(\vec{x}) = \partial^{k+l}|\tilde{\psi}(\vec{x})|^2/\partial x^k \partial y^l$ are derivatives of the incoherent PSF. Eqs. (6) and (7) reveal a quadratic scaling suboptimality in direct imaging —$\xi_{\mathrm{direct}}^{(1)} \sim \gamma^4$ vs $\xi_Q^{(1)} \sim \gamma^2$—for *all* binary discrimination tasks [38]. Alternatively, we analyze a "TRISPADE" measurement [Fig. 1(b)] [28] that sorts the collected light between the PSF-matched spatial mode and the first-order PAD-basis modes in two perpendicular dimensions. TRISPADE uses linear optics and shot-noise-limited photodetectors to implement a measurement with the object-independent projectors $\Pi_i = |\phi_i\rangle\langle\phi_i|$, $i \in [0,2]$. The resulting CE $\xi_{\mathrm{TRISPADE}}^{(1)}$ achieves the QCE when $\gamma \ll 1$ [22], so TRISPADE is a quantum-optimal measurement for binary sub-Rayleigh object discrimination.

In Fig. 3 we numerically evaluate $\xi_Q^{(1)}$, $\xi_{\mathrm{direct}}^{(1)}$, and $\xi_{\mathrm{TRISPADE}}^{(1)}$ from Eqs. (3) and (4) for the examples depicted in Fig. 2. We observe that the lowest-order $O(\gamma^2)$ behavior of the QCE, found by numerically maximizing Eq. (6), is an excellent approximation for both the QCE and the TRISPADE CE throughout the sub-Rayleigh regime ($\gamma < 1$). Meanwhile, Eq. (7) closely follows the $O(\gamma^4)$ sub-Rayleigh direct imaging CE, illustrating the general $O(\gamma^2)$ scaling gap. We also find TRISPADE to be robust to mode-sorter misalignment from the object centroid, retaining the $O(\gamma^2)$ advantage over direct imaging [Fig. 3(c)]. These results suggest that TRISPADE can perform a wide range of sub-Rayleigh hypothesis tests with substantially less error than conventional methods.

Results: M-ary object discrimination.—We now extend our analysis to $M > 2$ equiprobable objects, such as a library of quick response (QR) codes [Fig. 2(d)]. The M-ary QCE $\xi_{Q,M}^{(1)} = \min_{i \ne j}\xi_{Q,i,j}^{(1)}$, which characterizes the quantum-limited asymptotic error for discriminating M states, is found by minimizing the pairwise QCEs $\xi_{Q,i,j}^{(1)}$ for each pair of states $\{\rho_i, \rho_j\}$ [39]. The similarly defined M-ary CE
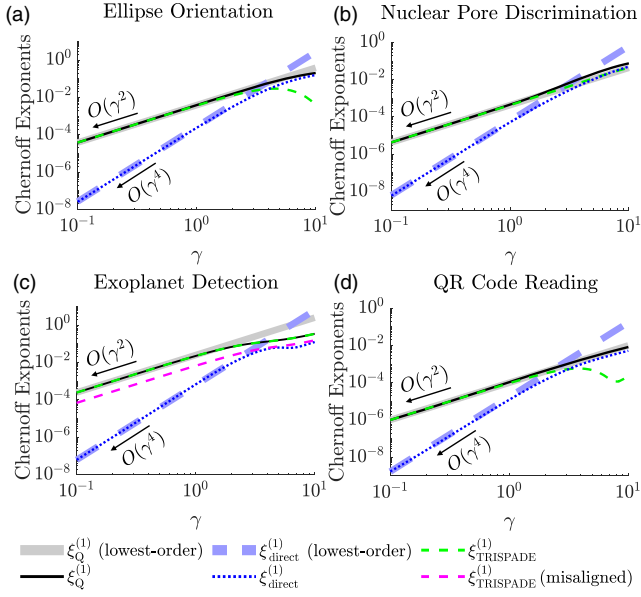
FIG. 3. (Q)CEs for the tasks in Fig. 2 with a Gaussian PSF. Thick lines: lowest-order (in γ) approximations for $\xi_Q^{(1)}$ [Eq. (6)] and $\xi_{\text{direct}}^{(1)}$ [Eq. (7)]. Thin lines: exact numerical results for $\xi_Q^{(1)}$ [Eq. (3)], $\xi_{\text{direct}}^{(1)}$ [Eq. (4)], and $\xi_{\text{TRISPADE}}^{(1)}$ [Eq. (4)]. Misalignment was $\theta/10$ for the misaligned $\xi_{\text{TRISPADE}}^{(1)}$ in c.

$\xi_{\text{meas},M}^{(1)} = \min_{i \neq j} \xi_{\text{meas},i,j}^{(1)}$ obeys the multiple quantum Chernoff bound $\xi_{\text{meas},M}^{(1)} \leq \xi_{Q,M}^{(1)}$ [39]. We have shown that TRISPADE saturates the quantum limit ($\xi_{\text{TRISPADE},i,j}^{(1)} = \xi_{Q,i,j}^{(1)}$) for any two states when $\gamma \ll 1$. Therefore, the TRISPADE measurement, which crucially does not depend on the candidate states, will always *simultaneously* achieve the QCE for all pairs of states in a library when $\gamma \ll 1$. It follows that TRISPADE saturates the multiple quantum Chernoff bound (i.e., $\xi_{\text{TRISPADE},M}^{(1)} = \xi_{Q,M}^{(1)}$) and is therefore a quantum-optimal measurement for discriminating within *any* M-object library in the sub-Rayleigh limit.

Furthermore, we identify "distance" measures that determine the prefactors of $\xi_{Q,M}^{(1)} \sim \gamma^2$ and $\xi_{\text{direct},M}^{(1)} \sim \gamma^4$ from the minimum distance among all object pairs in a library. Our measures, which depend on the second moments (m_{j,x^2} and m_{j,y^2}) of the candidate objects, resemble the Hamming distance in linear coding theory, which quantifies the distinguishability of noise-corrupted codewords [40]. Approximating Eq. (6) using the quantum Bhattacharyya bound [41], we find that relative square roots of object second moments (e.g., $\sqrt{m_{i,x^2}} - \sqrt{m_{j,x^2}}$) form a distance for the pairwise QCEs, such that $M = M_x M_y$ quadratically packed objects on a $M_x \times M_y$ rectangular grid within the 2D space of second moments [Fig. 4(a)] form an "equidistant" library, i.e., $\xi_{Q,i,j}^{(1)}$ is the
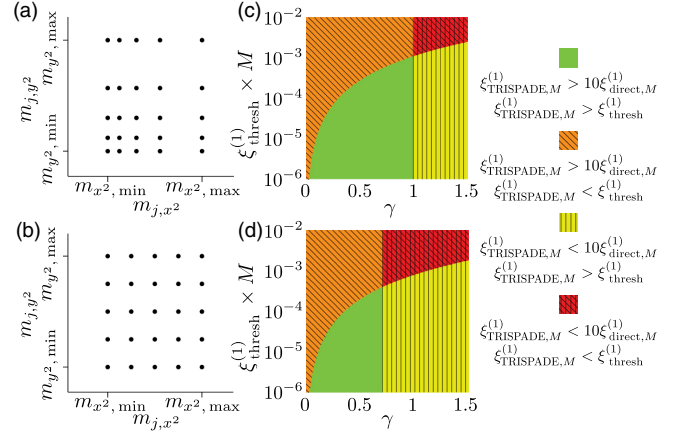

FIG. 4. (a) and (b) Visualization of generalized object libraries with quadratically and linearly packed 2D second moments. (c) and (d) Comparison of the CEs for TRISPADE, direct imaging, and an error threshold for M-ary object discrimination with a 2D Gaussian aperture to lowest order in γ ($m_{x^2,\min} = 0.05$, $m_{x^2,\max} = 0.1$).

same for all nearest-neighbor object pairs along either x or y [22]. Consider an equidistant library of objects constrained by $m_{x^2,\min} \leq m_{j,x^2} \leq m_{x^2,\max}$ and $m_{y^2,\min} \leq m_{j,y^2} \leq m_{y^2,\max}$ and let $M_x^2 = M_y^2 = M \gg 1$. Up to a coordinate rotation [22],

$$\xi_{Q,M}^{(1)} \approx \frac{(\sqrt{m_{x^2,\max}} - \sqrt{m_{x^2,\min}})^2 \Gamma_{x^2}}{2M} \gamma^2 + O(\gamma^3), \quad (8)$$

$$\xi_{\text{direct},M}^{(1)} = \frac{(\sqrt{m_{x^2,\max}} - \sqrt{m_{x^2,\min}})^2 \Psi_{x^2}}{8M m_{x^2,\min}^{-1}} \gamma^4 + O(\gamma^5), \quad (9)$$

where $\Psi_{x^2} = \int \int_{-\infty}^{\infty} \psi_{x^2}(\vec{x})^2 / |\tilde{\psi}(\vec{x})|^2 d^2\vec{x}$. For direct imaging, the differences $m_{i,x^2} - m_{j,x^2}$ constitute a distance measure for $\xi_{\text{direct},M}^{(1)}$ [Eq. (7)], so linearly packed objects form an equidistant library [Fig. 4(b)]. In this case [22],

$$\xi_{Q,M}^{(1)} \approx \frac{(m_{x^2,\max} - m_{x^2,\min})^2 \Gamma_{x^2}}{8M m_{x^2,\max}} \gamma^2 + O(\gamma^3), \quad (10)$$

$$\xi_{\text{direct},M}^{(1)} = \frac{(m_{x^2,\max} - m_{x^2,\min})^2 \Psi_{x^2}}{32M} \gamma^4 + O(\gamma^5). \quad (11)$$

To unravel the implications of these second-moment distances, we probe conditions under which the quantum-optimal TRISPADE receiver achieves a useful performance gain over conventional imaging. Figures 4(c) and 4(d) depict parametrized regions indicating whether, to lowest order in γ, the TRISPADE CE exceeds that of direct imaging by 1 order of magnitude (i.e., $\xi_{\text{TRISPADE},M}^{(1)} > 10\xi_{\text{direct},M}^{(1)}$) and/or satisfies a threshold
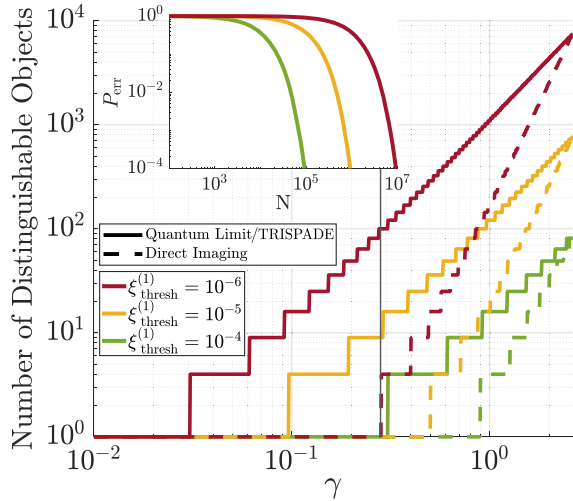
FIG. 5. Maximum number of objects that are distinguishable at a threshold error rate to lowest order in γ with a 2D Gaussian aperture ($m_{x^2,\min} = 0.05$, $m_{x^2,\max} = 0.1$). Inset: error probability vs mean detected photon number.

representing an acceptable application-specific error rate (i.e., $\xi^{(1)}_{\text{TRISPADE},M} > \xi^{(1)}_{\text{thresh}}$). We observe that γ determines the relative improvement over direct imaging, and quadratic object packing (c) yields the 10x improvement for a larger slice of the sub-Rayleigh regime than linear packing (d), highlighting the different distance measures between the two measurements. Satisfying the error threshold $\xi^{(1)}_{\text{thresh}}$ requires a tradeoff with γ and the number of objects M but is less sensitive to the second-moment packing configuration of the library.

Finally, in Fig. 5 we ask how many objects can be distinguished to a desired accuracy with a conventional or quantum-optimal measurement, which directly relates to the decision-making power of an imaging system. Using an equidistant library for both measurements, we solve Eqs. (8) and (11) for M and find that TRISPADE distinguishes more objects than direct imaging by an increasing factor as γ decreases for any threshold error rate. For instance, at a relaxed threshold $\xi^{(1)}_{\text{thresh}} = 10^{-6}$, i.e., higher tolerable error and/or more available photons (inset), TRISPADE distinguishes 100 objects at $\gamma = 0.28$ (vertical line), while direct imaging cannot identify more than one. We conclude that TRISPADE significantly increases the complexity of distinguishable sub-Rayleigh object libraries without compromising performance.

Conclusion.—Our Letter shows that a simple optical receiver could enable substantial improvements in decision making in many superresolution imaging contexts. System imperfections (e.g., optical losses, mode crosstalk, detector noise) and limited prior knowledge of the library (e.g., object defects, unknown pose) are outside the scope of this Letter but can only reduce discrimination accuracy from the ideal case [42,43]. Our quantum limit is therefore a

fundamental lower bound on identification error that can rule out quantitative regimes of discrimination capability for future imaging systems.

[1] L. Rayleigh, Investigations in optics, with special reference to the spectroscope, Philos. Mag. **8**, 261 (1879).

[2] J. W. Goodman, *Introduction to Fourier Optics*, 3rd ed. (Roberts and Company, Englewood, CO, USA, 2005).

[3] M. Tsang, Resolving starlight: A quantum perspective, Contemp. Phys. **60**, 279 (2020).

[4] M. Tsang, R. Nair, and X. M. Lu, Quantum Theory of Superresolution for Two Incoherent Optical Point Sources, Phys. Rev. X **6**, 031033 (2016).

[5] Z. Dutton, R. Kerviche, A. Ashok, and S. Guha, Attaining the quantum limit of superresolution in imaging an object's length via predetection spatial-mode sorting, Phys. Rev. A **99**, 033847 (2019).

[6] M. Tsang, Quantum limit to subdiffraction incoherent optical imaging, Phys. Rev. A **99**, 012305 (2019).

[7] S. Zhou and L. Jiang, A modern description of Rayleigh's criterion, Phys. Rev. A **99**, 013808 (2019).

[8] C. Lupo, Z. Huang, and P. Kok, Quantum Limits to Incoherent Imaging are Achieved by Linear Interferometry, Phys. Rev. Lett. **124**, 080503 (2020).

[9] X. M. Lu, H. Krovi, R. Nair, S. Guha, and J. H. Shapiro, Quantum-optimal detection of one-versus-two incoherent optical sources with arbitrary separation, npj Quantum Inf. **4**, 64 (2018).

[10] H. Zhang, S. Kumar, and Y.-P. Huang, Super-resolution optical classifier with high photon efficiency, Opt. Lett. **45**, 4968 (2020).

[11] Z. Huang and C. Lupo, Quantum Hypothesis Testing for Exoplanet Detection, Phys. Rev. Lett. **127**, 130502 (2021).

[12] U. Zanforlin, C. Lupo, P. W. R. Connolly, P. Kok, G. S. Buller, and Z. Huang, Optical quantum super-resolution imaging and hypothesis testing, arXiv:2202.09406.

[13] L. Mandel, Fluctuations of photon beams: The distribution of the photo-electrons, Proc. Phys. Soc. **74**, 233 (1959).

[14] M. Tsang, Subdiffraction incoherent optical imaging via spatial-mode demultiplexing, New J. Phys. **19**, 023054 (2017).

[15] Our perturbation theory for quantum information [16] will enable generalized results on asymmetric object discrimination via the quantum Stein lemma in future work.

[16] M. R. Grace and S. Guha, Perturbation theory for quantum information, arXiv:2106.05533.

[17] H. L. Van Trees and K. Bell, *Detection Estimation and Modulation Theory, Part I: Detection, Estimation, and*

Filtering Theory, 2nd ed. (John Wiley & Sons, Hoboken, New Jersey, 2013).

[18] K. M. R. Audenaert, J. Calsamiglia, R. Muñoz-Tapia, E. Bagan, L. Masanes, A. Acin, and F. Verstraete, Discriminating States: The Quantum Chernoff Bound, Phys. Rev. Lett. **98**, 160501 (2007).

[19] M. Nussbaum and A. Szkoła, The Chernoff lower bound for symmetric quantum hypothesis testing, Ann. Stat. **37**, 1040 (2009).

[20] C. W. Helstrom, *Quantum Detection and Estimation Theory* (Academic Press, Inc., New York, 1976).

[21] N. Yu and L. Zhou, When is the Chernoff exponent for quantum operations finite?, IEEE Trans. Inf. Theory **67**, 4517 (2021).

[22] See Supplemental Material at http://link.aps.org/supplemental/10.1103/PhysRevLett.129.180502 for derivations of analytical results, which includes Refs. [23–26].

[23] V. Kargin, On the Chernoff bound for efficiency of quantum hypothesis testing, Ann. Stat. **33**, 959 (2005).

[24] M. Paúr, B. Stoklasa, D. Koutný, J. Řeháček, Z. Hradil, J. Grover, A. Krzic, and L. L. Sánchez-Soto, Reading out Fisher information from the zeros of the point spread function, Opt. Lett. **44**, 3114 (2019).

[25] R. Nair and M. Tsang, Interferometric superlocalization of two incoherent optical point sources, Opt. Express **24**, 3684 (2016).

[26] H. T. Croft, K. J. Falconer, and R. K. Guy, *Unsolved Problems in Geometry*, 1st ed. (Springer, New York, 1991), pp. 108–110.

[27] The QCE optimizes over all POVMs including measurements that act collectively on multiple copies of the state η_j. For the present context, we show that individual measurements on each copy of η_j are sufficient to saturate the quantum Chernoff bound.

[28] S. Z. Ang, R. Nair, and M. Tsang, Quantum limit for two-dimensional resolution of two incoherent optical point sources, Phys. Rev. A **95**, 063847 (2017).

[29] P. Boucher, C. Fabre, G. Labroille, and N. Treps, Spatial optical mode demultiplexing as a practical tool for optimal transverse distance estimation, Optica **7** (2020).

[30] A. Sajjad, M. R. Grace, Q. Zhuang, and S. Guha, Attaining quantum limited precision of localizing an object in passive imaging, Phys. Rev. A **104**, 022410 (2021).

[31] M. R. Grace, Z. Dutton, A. Ashok, and S. Guha, Approaching quantum-limited imaging resolution without prior knowledge of the object location, J. Opt. Soc. Am. A **37**, 1288 (2020).

[32] J. O. de Almeida, J. Kolodynski, C. Hirche, M. Lewenstein, and M. Skotiniotis, Discrimination and estimation of incoherent sources under misalignment, Phys. Rev. A **103**, 022406 (2021).

[33] J. V. Thevathasan *et al.*, Nuclear pores as versatile reference standards for quantitative superresolution microscopy, Nat. Methods **16**, 1045 (2019).

[34] R. Kerviche, S. Guha, and A. Ashok, Fundamental limit of resolving two point sources limited by an arbitrary point spread function, in *2017 IEEE International Symposium on Information Theory (ISIT)* (IEEE, New York, 2017), pp. 441–445.

[35] J. Rehacek, M. Paúr, B. Stoklasa, Z. Hradil, and L. L. Sanchez-Soto, Optimal measurements for resolution beyond the rayleigh limit, Opt. Lett. **42**, 231 (2017).

[36] M. Tsang, Subdiffraction incoherent optical imaging via spatial-mode demultiplexing: Semiclassical treatment, Phys. Rev. A **97**, 023830 (2018).

[37] While Eq. (7) does not hold for PSFs that are zero-valued at one or more locations (e.g., the common Airy disk PSF), the scaling $\xi_{\mathrm{direct}}^{(1)} \sim \gamma^4$ is retained in this case [22].

[38] We analyze caveats regarding PSFs with zeros as well as object pairs with identical second moments or different first moments in [22]. These special cases maintain the qualitative features of our results. We find that the relative performance gap between $\xi_{\mathrm{Q}}^{(1)}$ and $\xi_{\mathrm{direct}}^{(1)}$ generally increases for more difficult discrimination tasks.

[39] K. Li, Discriminating quantum states: The multiple Chernoff distance, Ann. Stat. **44**, 1661 (2016).

[40] R. W. Hamming, Error detecting and error correcting codes, Bell Syst. Tech. J. **29**, 147 (1950).

[41] S. Pirandola and S. Lloyd, Computable bounds for the discrimination of gaussian states, Phys. Rev. A **78**, 012331 (2008).

[42] K. M. Audenaert and M. Mosonyi, Upper bounds on the error probabilities and asymptotic error exponents in quantum multiple state discrimination, J. Math. Phys. (N.Y.) **55**, 102201 (2014).

[43] M. Mosonyi, Z. Szilágyi, and M. Weiner, On the error exponents of binary quantum state discrimination with composite hypotheses, arXiv:2011.04645.